


Cite this: *RSC Adv.*, 2025, 15, 20111

# Design of a magnetic Fenton-like catalyst by decorating diamond-shaped MIL-88A with *Chenopodium*-derived biochar for nitrophenol degradation: optimization and mechanistic insights†

Abdelazeem S. Eltaweil,<sup>a</sup> Mohammed Salah Ayoub,<sup>b</sup> Jawaher Y. Al Nawah<sup>b</sup> and Eman M. Abd El-Monaem<sup>c</sup>

An effective Fenton-like  $\text{Fe}_3\text{O}_4/\text{MIL-88A/BC}$  catalyst was fabricated by combining magnetite nanoparticles ( $\text{Fe}_3\text{O}_4$ ) with diamond-shaped MIL-88A and *Chenopodium*-derived biochar for the degradation of 2-NP. The elemental composition, morphology, functional groups, surface net charge, and crystallographic phase of the  $\text{Fe}_3\text{O}_4/\text{MIL-88A/BC}$  catalyst were examined using various characterization techniques, including XPS, SEM, FTIR, ZP, and XRD. Optimization experiments were conducted to determine the optimal Fenton-like degradation conditions for 2-NP using  $\text{H}_2\text{O}_2/\text{Fe}_3\text{O}_4/\text{MIL-88A/BC}$ . Laboratory experiments showed that the 2-NP degradation efficiency by  $\text{H}_2\text{O}_2/\text{Fe}_3\text{O}_4/\text{MIL-88A/BC}$  reached 91.04% within 120 min at pH = 5,  $\text{Fe}_3\text{O}_4/\text{MIL-88A/BC}$  = 10 mg, and  $\text{H}_2\text{O}_2$  concentration = 500 mg  $\text{L}^{-1}$ . Kinetic studies indicated that the Fenton-like degradation of 2-NP followed a second-order model, while  $\text{H}_2\text{O}_2$  decomposition was best described by a first-order model. Quenching tests indicated that the Fenton-like reaction of 2-NP proceeded via a radical mechanism and confirmed that the  $\cdot\text{OH}$  radicals are the controlling reactive O-species. The degradation mechanism of 2-NP was proposed based on the XPS spectra of the neat and used  $\text{Fe}_3\text{O}_4/\text{MIL-88A/BC}$  catalysts. The intermediates obtained from the Fenton-like degradation of 2-NP by the  $\text{Fe}_3\text{O}_4/\text{MIL-88A/BC}$  catalyst were predicted from the GC-MS spectrum.

Received 12th April 2025  
Accepted 19th May 2025

DOI: 10.1039/d5ra02562a

rsc.li/rsc-advances

## 1. Introduction

Recently, the world has delved deeply into the issue of water pollution, which threatens the survival of human beings and the entire planet. Scientists and environmental experts are challenged by this dilemma because most water contaminants are cogs in the wheel of vital industries. For instance, 2-NP is widely used in numerous industries, including fungicide, petrochemical, pigment, explosive, pharmaceutical, insecticide, chemical intermediate, and herbicide industries. The total annual production of 2-NP ranges from 10 to 15 million pounds.<sup>1</sup> Nonetheless, the leakage of even a relatively low concentration of 2-NP into water bodies could lead to harmful effects on human health, such as blurred vision, liver and

kidney damage, drowsiness, mouth irritation, and cyanosis.<sup>2</sup> In addition, 2-NP has a disruptive impact on the environment, with its nitro-containing group contributing to its stability in water and soil.<sup>3</sup> Therefore, there is an essential need to investigate effective measures for controlling the presence of 2-NP in water bodies. Techniques such as adsorption, membrane filtration, electrolysis, coagulation, and Fenton degradation have progressed as promising approaches to tackle such hazardous compounds.<sup>4,5</sup>

The non-toxicity, plentiful iron sources, absence of secondary contaminant formation, and use of green oxidants make Fenton degradation a felicitous strategy to outdo 2-NP from wastewater.<sup>6</sup> Fenton reaction is one of the most efficacious hydroxyl radical-based advanced oxidation processes and has exhibited preeminent performance in degrading the notorious 2-NP. Generally, Fenton degradation of such persistent nitro-aromatic compounds proceeds via the formation of hydroxyl radicals ( $\cdot\text{OH}$ ) by the activation of hydrogen peroxide ( $\text{H}_2\text{O}_2$ ) using iron-based catalysts.<sup>7,8</sup> However, iron-based catalysts still require further development to enhance the production of  $\cdot\text{OH}$  radicals and accelerate the  $\text{Fe}^{2+}/\text{Fe}^{3+}$  cycle.

Metal-organic frameworks (MOFs) are considered a recent breakthrough in material science revolution. The discernible

<sup>a</sup>Chemistry Department, Faculty of Science, Alexandria University, Alexandria, Egypt. E-mail: abdelazeemeltaweil@alexu.edu.eg

<sup>b</sup>Department of Chemistry, College of Science, King Faisal University, Al-Ahsa 31982, Saudi Arabia. E-mail: jalnawah@kfu.edu.sa; mayoup@kfu.edu.sa

<sup>c</sup>Advanced Technology Innovation, Borg El-Arab, Alexandria, Egypt. E-mail: emanabdelmonaem5925@yahoo.com

† Electronic supplementary information (ESI) available. See DOI: <https://doi.org/10.1039/d5ra02562a>


characteristics of MOFs, such as excellent thermal and mechanical properties, high surface area, and high porosity, render them appropriate for numerous applications, including drug delivery, sensors, gas separation, wastewater purification, and solar cells.<sup>9,10</sup> For wastewater purification, MOFs have demonstrated outstanding results in removing persistent pollutants *via* many remediation strategies. In particular, Fenton degradation is due to the individual chemical structures of the ligands, which contain unsaturated coordination species and abundant oxygen functional groups.<sup>11</sup> Iron-based MOFs, including MIL-101, MIL-88A, MIL-100, MIL-88B, and MIL-53, have demonstrated remarkable performance in degrading diverse contaminants by the Fenton degradation process. In particular, MIL-88A has gained exceptional interest as a remarkable Fenton catalyst owing to its high recyclability, efficient catalytic activity, and chemical stability.<sup>12</sup>

Biochar (BC) is a dust-carbon-rich substance derived from biowaste *via* thermal decomposition under pyrolysis temperatures in the range of 300–900 °C.<sup>13,14</sup> Interestingly, the conversion of biowaste, like agricultural waste, to BC could provide a better solution for removing this waste instead of burning it. Reported studies have demonstrated the hazardous impact of burning agricultural waste on human health, especially the respiratory system.<sup>15</sup> Thanks to the remarkable properties of BC, such as good mechanical strength, porous structure, high surface area, and possession of oxygenated groups, it makes it a superb catalyst for degrading pollutants by Fenton/Fenton-like reactions.<sup>16</sup> In addition, environmentally persistent free radicals (EPFRs)-containing BC can activate H<sub>2</sub>O<sub>2</sub> to generate <sup>•</sup>OH radicals during Fenton/Fenton-like reactions.<sup>17</sup>

Magnetite (Fe<sub>3</sub>O<sub>4</sub>) is a bright iron-based nanocatalyst that has demonstrated remarkable performance in Fenton degradation reactions of many harmful pollutants.<sup>18</sup> This auspicious catalytic performance of Fe<sub>3</sub>O<sub>4</sub> stems from its Fe<sup>2+</sup> ions, which activate H<sub>2</sub>O<sub>2</sub> *via* the Haber–Weiss reaction and produce <sup>•</sup>OH radicals.<sup>19</sup> Fe<sub>3</sub>O<sub>4</sub> possesses an excellent ferromagnetic character, resulting in easy separation features that prevent mass loss during regeneration and save time during the separation step.<sup>20</sup> Additionally, Fe<sub>3</sub>O<sub>4</sub> is a non-toxic substance with a wide surface area, good chemical stability, intrinsic peroxidase, and propitious recyclability.<sup>21,22</sup> Notably, the octahedral site in the Fe<sub>3</sub>O<sub>4</sub> matrix allows it to accommodate Fe<sup>2+</sup> and Fe<sup>3+</sup>; therefore, the Fe<sup>2+</sup> moieties can be oxidized reversibly by transferring electrons between Fe<sup>2+</sup> and Fe<sup>3+</sup>.<sup>23,24</sup>

The MIL-88A and/or BC-based heterogeneous catalysts exhibit eminent catalytic activity in Fenton degradation reactions of various organic contaminants. For instance, Ren *et al.* fabricated ZnO-decorated MIL-88A rods to degrade methylene blue, clarifying that the degradation percentage attained 96.15% after a reaction time of 40 min.<sup>25</sup> Abd El-Monaem *et al.* developed rod-shaped MIL-88A with SnFe<sub>2</sub>O<sub>4</sub> and supported them on MXene sheets for degrading the anionic Congo red dye, achieving a promising degradation percentage of 100% after 60 min. In addition, the synergistic effect of the CR adsorption and the Fenton-like process was monitored, where the adsorption percentage of CR was 47.25%.<sup>26</sup> Liao and his coworkers compared the catalytic activity of rod, diamond, and spindle-

shaped MIL-88A toward the Fenton degradation of phenol. The experimental findings demonstrated that the catalytic degradation efficiency of the rod-like MIL-88A toward phenol was higher than that of the other forms, where it fulfilled 100% after 15 min.<sup>27</sup> Moreover, Sang *et al.* study involved investigating the Fenton-like degradation of ciprofloxacin by natural pyrite/rice straw-derived biochar, revealing that the degradation percentage achieved 96.8% after 20 minutes.<sup>28</sup> Park and his coauthors fabricated Fe-impregnated sugarcane biochar for degrading Orange G throughout a Fenton-like reaction. The degradation percentage of Orange G reached 99.70% after 120 minutes using 0.5 g L<sup>-1</sup> of the Fe-impregnated biochar at pH = 5.5.<sup>29</sup>

In light of previous studies, diamond-shaped MIL-88A and BC were not used to degrade o-NP by the Fenton-like reaction. Meanwhile, MIL-88A and BC exhibit high dispersity, which hinders their separation from the catalytic media after Fenton reactions. To overcome the high dispersity of MIL-88A and BC, they can be incorporated into polymeric materials and shaped into beads, hydrogels, or membranes. However, the degradation efficacy may decline because of the lower catalytic activity of the polymers. On the other hand, adding a magnetic substance to MIL-88A and BC results in a magnetic catalyst that can be separated perfectly from the catalytic media by an external magnet. Magnetic substances contain transition metals that exhibit remarkable activity toward degrading organic pollutants *via* Fenton/Fenton-like reactions.

Accordingly, our investigation aimed to take the merits of MIL-88A, Fe<sub>3</sub>O<sub>4</sub>, and BC to fabricate a Fenton-like catalyst with eminent catalytic activity, excellent chemical stability, and outstanding recyclability. Consequently, an Fe<sub>3</sub>O<sub>4</sub>/MIL-88A/BC composite was prepared, and its chemical and physical properties were studied using varied characterization tools, including XPS, FTIR, VSM, ZP measurements, SEM, and XRD. The optimum Fenton-like parameters for degrading 2-NP by Fe<sub>3</sub>O<sub>4</sub>/MIL-88A/BC were investigated after a series of degradation reactions at different pH values, catalyst doses, 2-NP and H<sub>2</sub>O<sub>2</sub> concentrations, and temperatures. The kinetic models were applied to the experimental results obtained by degrading 2-NP and H<sub>2</sub>O<sub>2</sub> over time. The chemical stability of the Fenton-like Fe<sub>3</sub>O<sub>4</sub>/MIL-88A/BC catalyst was confirmed by cycling tests and metal leaching studies after each recycling run. The Fenton-like degradation mechanism of o-NP by H<sub>2</sub>O<sub>2</sub> activation using the Fe<sub>3</sub>O<sub>4</sub>/MIL-88A/BC catalyst was proposed based on the quenching test results and XPS spectra of fresh and used Fe<sub>3</sub>O<sub>4</sub>/MIL-88A/BC. The intermediates yielded from 2-NP degradation by Fe<sub>3</sub>O<sub>4</sub>/MIL-88A/BC were determined by GC-MS.

## 2. Materials and methods

### 2.1. Materials

The chemicals used in the preparation stage of the Fe<sub>3</sub>O<sub>4</sub>/MIL-88A/BC catalyst were Ferric chloride hexahydrate (FeCl<sub>3</sub>·6H<sub>2</sub>O) and fumaric acid (FA), which were purchased from Aladdin Industrial Corporation (China). Ferrous chloride tetrahydrate was obtained from Sigma-Aldrich (USA). Ammonium solution (NH<sub>4</sub>OH) and 2-NP were obtained from Sinopharm Chemical



Reagent (China). *N,N* dimethyl formamide (DMF) and ethanol ( $C_2H_5OH$ ) were obtained from Shanghai Chemical Reagent Co., Ltd (China).

## 2.2. Preparation of $Fe_3O_4$ /MIL-88A/BC catalyst

**2.2.1. Preparation of MIL-88A.** MIL-88A was fabricated using a solvothermal approach; in a beaker containing 50 mL DMF, 1.4 g of  $FeCl_3 \cdot 6H_2O$  was added under stirring until complete dissolution of the iron salt. Then, 0.52 g of FA was dipped into a bright orange solution containing  $Fe^{3+}$  ions while continuously stirring for 1 h. The obtained metal/ligand solution was poured into an autoclave and heated at 120 °C for one day. The formed MIL-88A particles were collected, washed with DMF and  $C_2H_5OH$ , and dried at 50 °C for 16 h in an oven.<sup>30</sup>

**2.2.2. Preparation of  $Fe_3O_4$ .** Magnetic  $Fe_3O_4$  was fabricated using the precipitation method under a nitrogen atmosphere. A solution of  $Fe^{3+}/Fe^{2+}$  ions was prepared by dissolving  $FeCl_3 \cdot 6H_2O$  and  $FeCl_2 \cdot 4H_2O$  in 200 mL of distilled water. Drops of  $NH_4OH$  were added slowly over the  $Fe^{3+}/Fe^{2+}$  solution until the pH reached 10, and then the chocolate brown particles were kept at 80 °C. After 90 min,  $Fe_3O_4$  nanoparticles were collected using a magnet, washed with distilled water and ethanol, and dried at 65 °C for 10 h.<sup>31</sup>

**2.2.3. Preparation of biochar.** *Chenopodium* plants were collected from agricultural land in El-Behara, Egypt. *Chenopodium* was thoroughly cleaned with tap water, followed by distilled water. The clean plant was kept in an oven at 70 °C until complete drying and then cut into small pieces (~1 cm). Finally, dried *Chenopodium* was pyrolyzed at 400 °C for 4 h under anoxic conditions. The obtained black powder of BC was ground using a mortar and pestle and stored in a glass tube.

**2.2.4. Preparation of  $Fe_3O_4$ /MIL-88A/BC composite.** The  $Fe_3O_4$ /MIL-88A/BC catalyst was prepared using a post-synthetic approach, as shown in Fig. 1. In a beaker containing 20 mL of distilled water, 100 mg of MIL-88A was added under sonication

for 30 min. Then, 20 mg of  $Fe_3O_4$  and amounts of BC (5–20 wt%) were mixed into the MIL-88A suspension *via* continual sonication for 2 h. The  $Fe_3O_4$ /MIL-88A/BC composites were dried at 50 °C for 6 h. After fabricating the  $Fe_3O_4$ , MIL-88A, BC, and  $Fe_3O_4$ /MIL-88A/BC composites, the physical and chemical characteristics of these samples were inspected using various characterization tools, as elucidated in Text S1.†

## 2.3. Fenton-like degradation experiment

The Fenton-like reaction of 2-NP by activating  $H_2O_2$  using an  $Fe_3O_4$ /MIL-88A/BC catalyst was studied as follows: (i) a comparison test between  $Fe_3O_4$ , MIL-88A, BC, and  $Fe_3O_4$ /MIL-88A/BC composites for evincing the synergistic effect between the composite's components and selecting the optimal BC proportion. (ii) Proceeding with the Fenton-like degradation of 2-NP at a pH range of 3–11 to pick out the optimum pH of the catalytic medium. (iii) Determine the economical dose of  $Fe_3O_4$ /MIL-88A/BC by proceeding with Fenton-like degradation of 2-NP using varied doses of the catalyst (5–20 mg). (iv) Studying the effect of oxidant concentration on the degradation aptitude of 2-NP at  $H_2O_2$  concentrations ranging from 100 to 1000  $mg\ L^{-1}$ . (v) Identifying the effect of the temperature of the  $Fe_3O_4$ /MIL-88A/BC- $H_2O_2$  catalytic system on the degradation efficacy of 2-NP. (vi) Investigating the influence of the 2-NP concentration (50–300  $mg\ L^{-1}$ ) on the degradation efficiency at the constant weight of  $Fe_3O_4$ /MIL-88A/BC. The undegraded 2-NP concentration was determined using a spectrophotometer at a maximum wavelength of 344 nm, and the degradation efficiency of 2-NP was estimated using eqn (1).

$$\text{Degradation efficiency, DE} = \frac{C_0 - C_t}{C_0} \times 100 \quad (1)$$

where  $C_0$  is the initial 2-NP concentration, and  $C_t$  is the undegraded concentration of 2-NP after the Fenton-like degradation process.

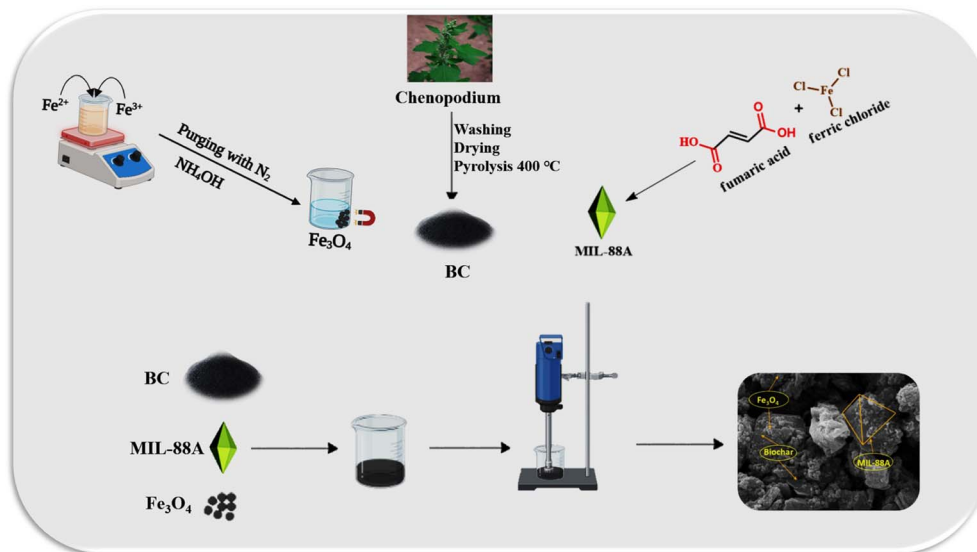


Fig. 1 Schematic representation of the fabrication process of the  $Fe_3O_4$ /MIL-88A/BC catalyst.



## 2.4. Cycling test

The regeneration potential of the  $\text{Fe}_3\text{O}_4/\text{MIL-88A}/\text{BC}$  catalyst was assessed by performing the cycling test for five cycles. After the Fenton-like degradation of 2-NP was completed, the  $\text{Fe}_3\text{O}_4/\text{MIL-88A}/\text{BC}$  catalyst was collected using a magnet, washed with an aqueous solution of NaOH (1 M) and distilled water, and dried at 50 °C in an oven. Subsequently, the regenerated  $\text{Fe}_3\text{O}_4/\text{MIL-88A}/\text{BC}$  catalyst was tested in the next Fenton-like degradation cycle of 2-NP.

## 2.5. Extraction of the intermediate compounds

The intermediate compounds from degrading 2-NP by  $\text{Fe}_3\text{O}_4/\text{MIL-88A}/\text{BC}$  were extracted from the Fenton-like catalytic medium by a liquid-liquid extraction procedure as follows: adding 20 mL of the 2-NP solution after the Fenton-like degradation reaction and 20 mL of  $\text{C}_4\text{H}_8\text{O}_2$  in a separatory funnel. After extracting the organic compounds, they were dried with  $\text{Na}_2\text{SO}_4$  using rotary evaporation. Next, the extracted sample was dissolved in MeOH and injected into the GC-MS (PE-5MS column; 0.18 mm film thickness, 0.18 mm diameter, and 20 m length) at 80 °C with the temperature increasing by 10 °C  $\text{min}^{-1}$  until reaching 280 °C.<sup>32</sup>

# 3. Results and discussion

## 3.1. Studying the $\text{Fe}_3\text{O}_4/\text{MIL-88A}/\text{BC}$ characteristics

Based on the experimental results, the  $\text{Fe}_3\text{O}_4/\text{MIL-88A}/\text{BC}$  composite containing 10 wt% BC exhibited the highest catalytic activity toward o-NP. Therefore, a characterization analysis was conducted on the catalyst containing 10 wt% BC.

**3.1.1. FTIR.** The chemical compositions and functional groups of the MIL-88A,  $\text{Fe}_3\text{O}_4$ , BC, and  $\text{Fe}_3\text{O}_4/\text{MIL-88A}/\text{BC}$  composites were investigated by FTIR analysis, as shown in Fig. 2A. The spectrum of MIL-88A shows FTIR peaks at the wavenumbers of 981 and 1213  $\text{cm}^{-1}$  related to C–C and C–H bonds of the trans diene of FA; in addition, the Fe–O peak manifests at the wavenumber of 554  $\text{cm}^{-1}$ . The C=O peaks of the carboxylate groups of FA appeared at wavenumbers of 1551  $\text{cm}^{-1}$  (asymmetric C=O) and 1398  $\text{cm}^{-1}$  (symmetric C=O). The wide-broad band between 3354 and 3514  $\text{cm}^{-1}$  is attributed to OH groups.<sup>23–25</sup> The FTIR spectrum of  $\text{Fe}_3\text{O}_4$  demonstrated the chemical functional groups of  $\text{Fe}_3\text{O}_4$ , which revealed the accredited peaks to Fe–O–Fe at wavenumbers of 559 and 1402  $\text{cm}^{-1}$ . In addition, the FTIR peaks of bending OH appeared at 1634  $\text{cm}^{-1}$ , and vibrating OH appeared at

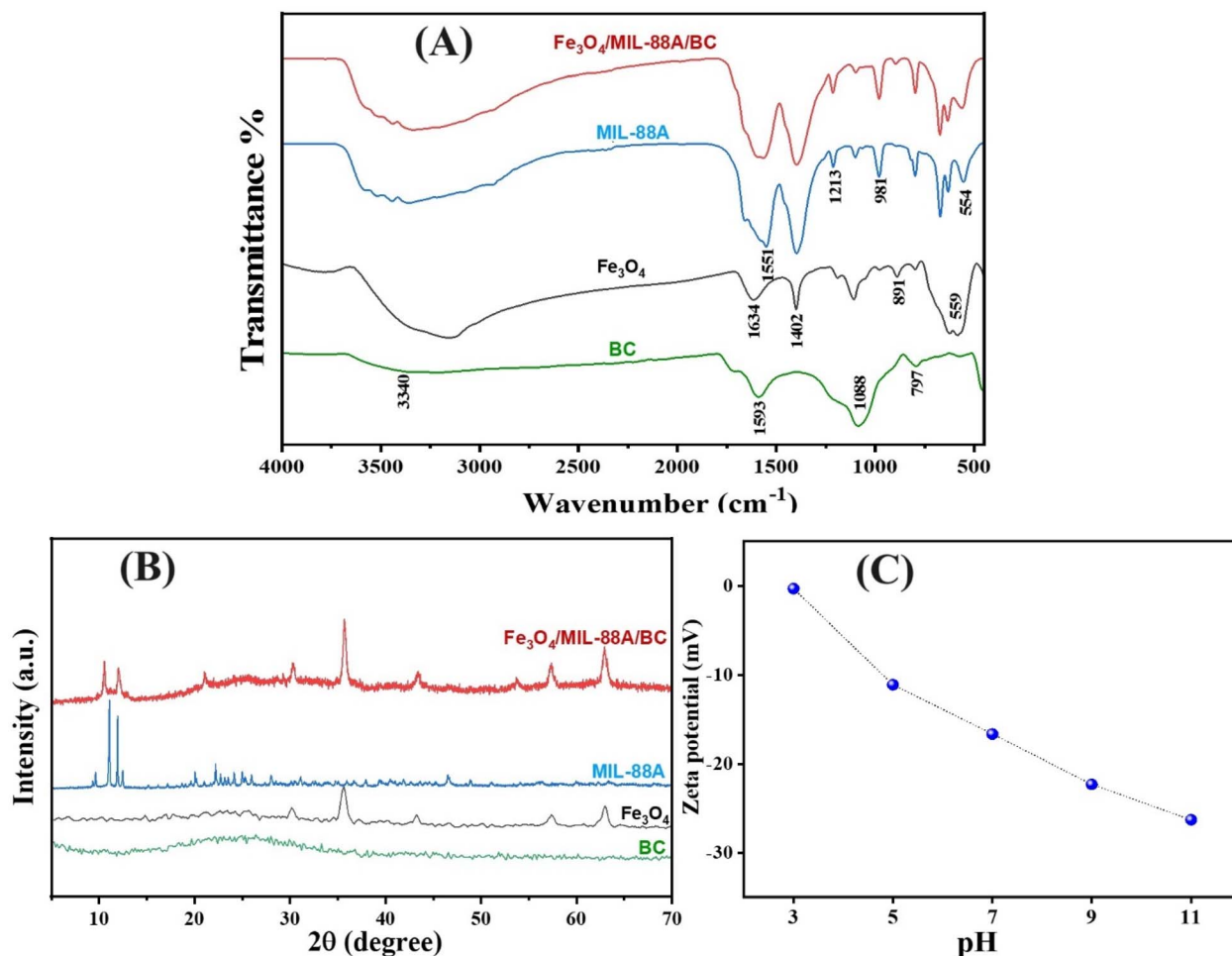


Fig. 2 (A) FTIR spectra, (B) XRD of MIL-88A,  $\text{Fe}_3\text{O}_4$ , BC, and  $\text{Fe}_3\text{O}_4/\text{MIL-88A}/\text{BC}$  composites, and (C) zeta potentials of the  $\text{Fe}_3\text{O}_4/\text{MIL-88A}/\text{BC}$  composites.





891  $\text{cm}^{-1}$ .<sup>26,27</sup> The spectrum of BC shows FTIR peaks at 458 and 1088  $\text{cm}^{-1}$ , which are assigned to Si-O and C-O, respectively. The C-H peak appeared at 797  $\text{cm}^{-1}$ , and the peak at 1593  $\text{cm}^{-1}$  corresponded to C=C.<sup>28</sup> The FTIR spectrum of the  $\text{Fe}_3\text{O}_4/\text{MIL-88A}/\text{BC}$  composite denoted the well-blending of MIL-88A,  $\text{Fe}_3\text{O}_4$ , and BC, where their distinguishing bands are obvious.

**3.1.2. XRD.** The crystallographic phases of the MIL-88A,  $\text{Fe}_3\text{O}_4$ , BC, and  $\text{Fe}_3\text{O}_4/\text{MIL-88A}/\text{BC}$  composites were determined from the XRD patterns (Fig. 2B). The crystalline pattern of MIL-88A shows distinct peaks at  $2\theta$  9.54°, 11.12°, 11.90°, 20.27°, 22.02°, and 24.03° corresponding to the planes 011, 101, 002, 201, 103, and 202, respectively.<sup>29</sup> The pattern of  $\text{Fe}_3\text{O}_4$  illustrates the XRD characteristic peaks at  $2\theta$  30.23°, 35.79°, 43.20°, 57.09°, and 62.79°, which belong to the 220, 311, 400, 511, and 440 planes, respectively. The XRD profile of the *Chenopodium*-based BC showed a broad peak between  $2\theta$  14.17° and 37.28°, indicating a typical amorphous structure of BC.<sup>2</sup> The pattern of the  $\text{Fe}_3\text{O}_4/\text{MIL-88A}/\text{BC}$  composite confirmed the combination of  $\text{Fe}_3\text{O}_4$ , MIL-88A, and BC, where the distinguishing peaks of MIL-88A and  $\text{Fe}_3\text{O}_4$  appeared with a slight shift and decline in their intensity, with the existence of the amorphous peak of BC at the same peak area.

**3.1.3. Zeta potential.** The amount of charge carried on the surface of the  $\text{Fe}_3\text{O}_4/\text{MIL-88A}/\text{BC}$  catalyst was investigated by zeta potential measurements (Fig. 2C). The results implied the existence of high negative charges on the catalyst's surface that increased with increasing pH from 3 to 11, where the zeta potential augmented from -0.315 to -26.30 eV sequentially. This high negative charge on the  $\text{Fe}_3\text{O}_4/\text{MIL-88A}/\text{BC}$  surface is most likely due to the oxygen-containing functional groups (*viz.*, COOH and OH) that share electrons during Fenton-like degradation to activate  $\text{H}_2\text{O}_2$  and yield  $\cdot\text{OH}$ .

**3.1.4. XPS.** The elemental compositions of the  $\text{Fe}_3\text{O}_4/\text{MIL-88A}/\text{BC}$  composites were determined by XPS analysis. The wide XPS spectrum exhibited three characteristic peaks for C 1s, Fe 2p, and O 1s at 285.99, 712.04, and 531.84 eV, respectively. The atomic percentages of carbon, iron, and oxygen were 49.56%, 8.57%, and 41.88%, respectively. The high resolution of O 1s (Fig. 3A) clarified the corresponding peak to the carboxylate group of FA at 531.15 eV; in addition, the peaks of Fe-O-Fe and C-O appeared at 529.56 and 531.18 eV, respectively. The high-resolution spectrum of C 1s (Fig. 3B) reveals the XPS peaks at 288.42 and 286.18 eV that are attributed to C=O and C-O, and the peak at 284.67 eV corresponds to C-H and C-C. The peaks located in the Fe 2P spectrum (Fig. 3C) at 710.35 and 712.47 eV

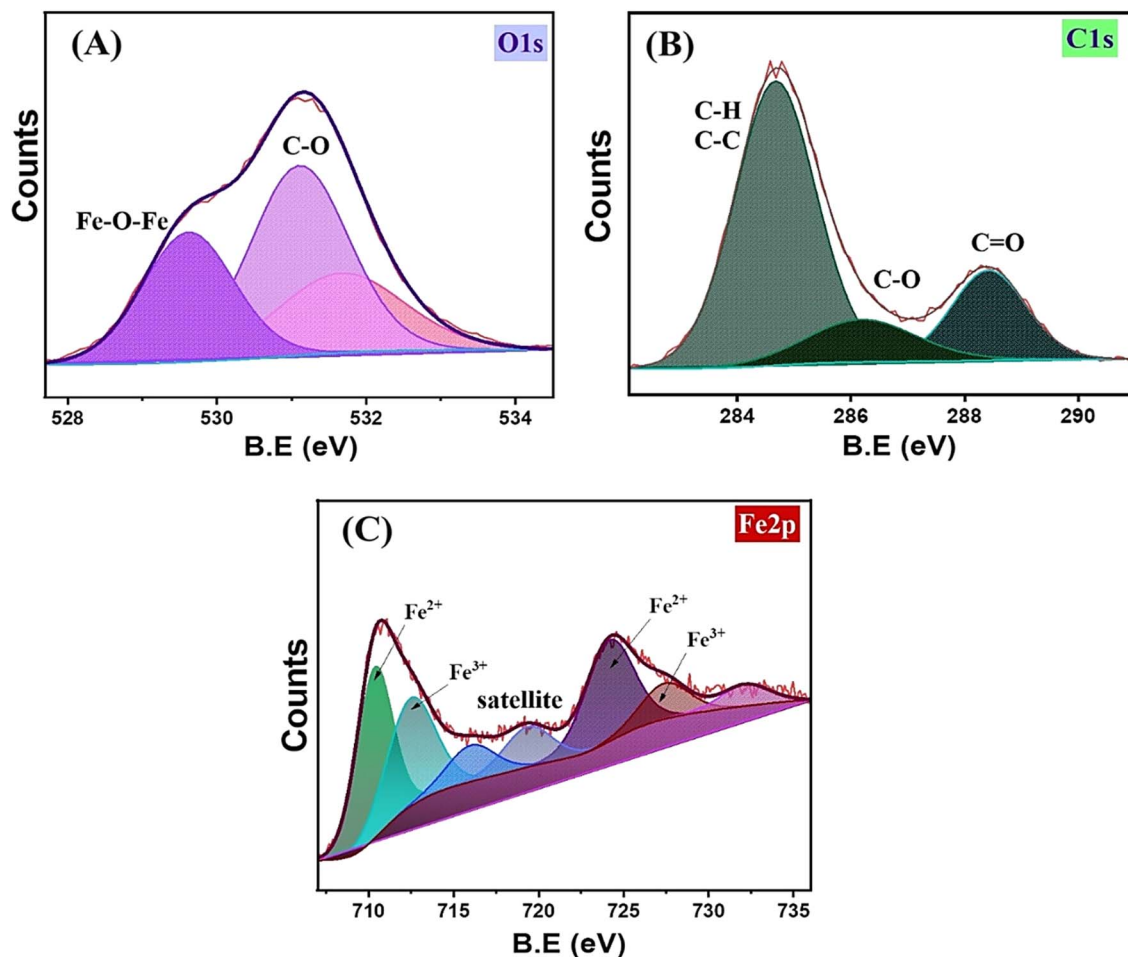


Fig. 3 XPS spectra of the  $\text{Fe}_3\text{O}_4/\text{MIL-88A}/\text{BC}$  composite: (A) O 1s, (B) C 1s, and (C) Fe 2p.

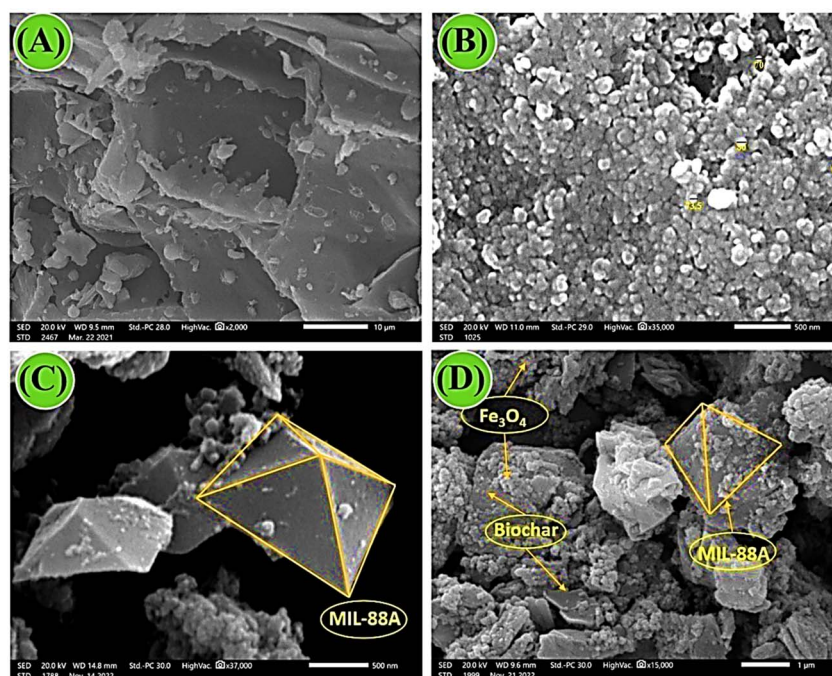


Fig. 4 SEM images of (A) BC, (B)  $\text{Fe}_3\text{O}_4$ , (C) MIL-88A, and (D)  $\text{Fe}_3\text{O}_4$ /MIL-88A/BC composite.

are assigned to  $\text{Fe}^{2+}$  and  $\text{Fe}^{3+}$  of  $\text{Fe}2\text{p}_{3/2}$ , respectively, and their satellite peaks exist at 716.01 and 719.36 eV. The XPS peaks of  $\text{Fe}2\text{p}_{1/2}$  at 724.16 and 727.42 eV belong to  $\text{Fe}^{2+}$  and  $\text{Fe}^{3+}$ , respectively, whereas the satellite peak appeared at 732.16 eV.

**3.1.5. SEM.** The SEM images (Fig. 4A–D) show the outer morphologies of the MIL-88A,  $\text{Fe}_3\text{O}_4$ , BC, and  $\text{Fe}_3\text{O}_4$ /MIL-88A/BC composites. The SEM image shows that the morphology of the BC surface is quite rough with some burs. This specification of the BC surface enables it to be a supporter of MIL-88A and  $\text{Fe}_3\text{O}_4$ . The  $\text{Fe}_3\text{O}_4$  morphology was manifested in the SEM images as quasi-spheroidal particles with nanoscale sizes. The SEM image shows the diamond-like morphology of MIL-88A, which is one of the most famous shapes of MIL-88A that is fabricated *via* a solvothermal approach using DMF as a solvent. The SEM of  $\text{Fe}_3\text{O}_4$ /MIL-88A/BC revealed clumps of  $\text{Fe}_3\text{O}_4$  on the diamond-like particles of MIL-88A supported on the surface of BC.

### 3.2. Optimizing the Fenton-like degradation process of 2NP

**3.2.1. Comparison test.** A series of Fenton-like degradation experiments on 2-NP (Fig. 5A) were conducted using  $\text{Fe}_3\text{O}_4$ , MIL-88A, BC, and  $\text{Fe}_3\text{O}_4$ /MIL-88A/BC composites as catalysts under the same reaction conditions. Additionally, the Fenton-like reaction of 2-NP was conducted using  $\text{H}_2\text{O}_2$  alone without the addition of a catalyst. An inferior DE of 2-NP was recorded in the presence of  $\text{H}_2\text{O}_2$  only (9.46%), suggesting the importance of the catalyst for activating  $\text{H}_2\text{O}_2$  and producing free radicals. The DE of 2-NP prepared using  $\text{Fe}_3\text{O}_4$ , MIL-88A, and BC was 46.05%, 63.75%, and 35.56%, respectively. Furthermore, the  $\text{Fe}_3\text{O}_4$ /MIL-88A/BC composites with varied proportions of BC exhibited degradation percentage of 2-NP by 58.51%, 64.05%, 80.25%,

and 71.97% when the doped BC amounts were 5, 7, 10, and 20 wt%. The former results demonstrated a synergistic effect between iron-based catalysts ( $\text{Fe}_3\text{O}_4$  and MIL-88A) and EPFR-containing BC, which work together to activate  $\text{H}_2\text{O}_2$  and generate  $\cdot\text{OH}$  radicals.<sup>17</sup> Moreover, it was noticed that there was an increment in the DE of 2-NP when the doped proportion of BC was augmented from 5 to 10 wt%, whereas the over-increment in the doped BC amount in the catalyst decreased the DE of 2-NP. This finding may be due to the aggregation of the excess proportion of BC, which diminished the available surface area of the  $\text{Fe}_3\text{O}_4$ /MIL-88A/BC catalyst.<sup>6</sup> Thus, the  $\text{Fe}_3\text{O}_4$ /MIL-88A/BC catalyst, which contained 10 wt% BC, was used to perform the rest of the o-NP Fenton-like degradation experiments.

**3.2.2. Influence of pH.** Since the Fenton-like process is quite sensitive to the pH of the catalytic reaction media, the Fenton-like degradation of 2-NP was examined in the pH range of 3–11, as illustrated in Fig. 5B. The experimental results showed that the best pH for degrading 2-NP was at a low acidic medium and near alkaline medium (DE = 80.25% at pH 5). In addition, a significant decline in the DE of 2-NP was observed in the presence of a lower acidic and higher alkaline media. These findings may be ascribed to the higher redox potential of  $\text{H}_2\text{O}_2$  in acidic medium ( $E^0 = 2.7$  eV) than in alkaline medium ( $E^0 = 1.8$  eV), so the  $\cdot\text{OH}$  radicals produced in a highly acidic medium are lower.<sup>33</sup> In addition, the abundant  $\text{H}^+$  in a highly acidic medium retards  $\cdot\text{OH}$  degradation during the reaction of 2-NP molecules. Moreover, a significant decline in the DE of 2-NP reached its half value under highly basic conditions, where the high concentrations of hydroxyl radicals resulted in the formation of hydro-peroxy anions with potent affinity toward



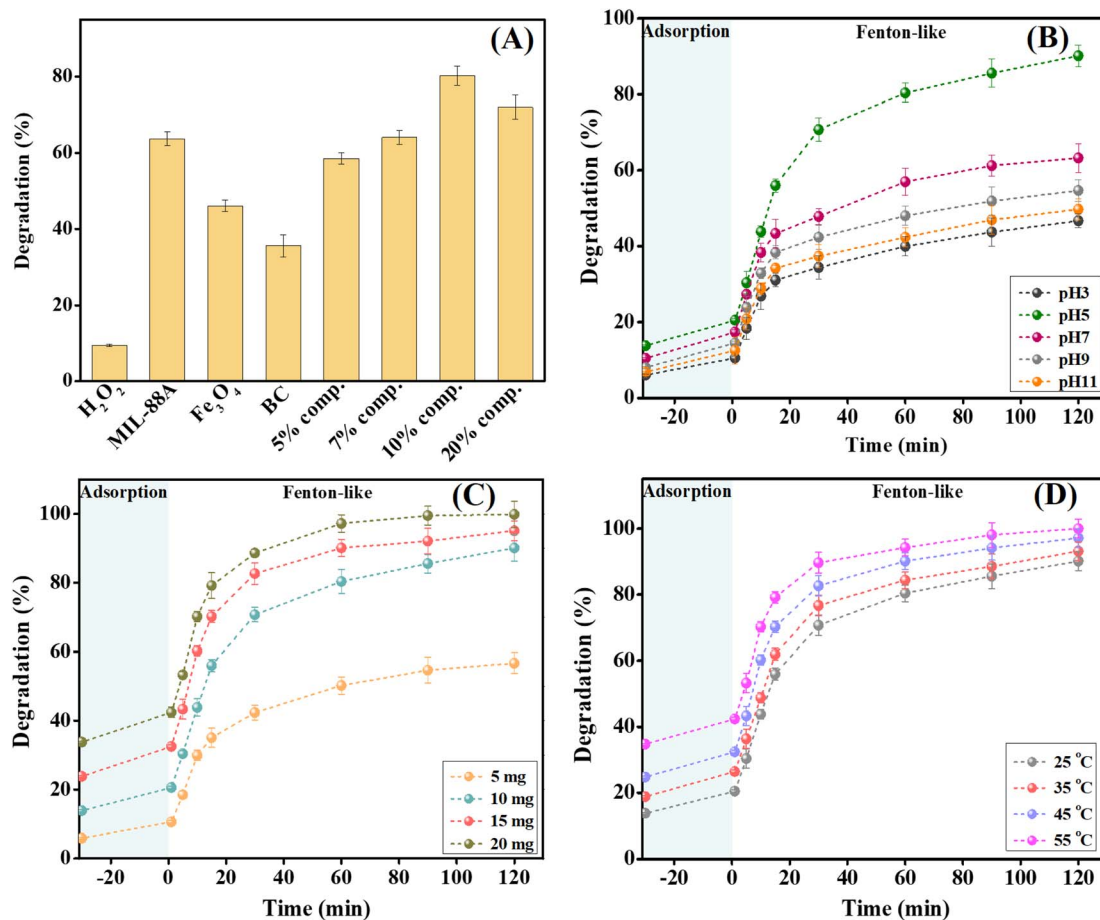
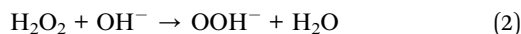


Fig. 5 (A) Comparison test (dose = 10 mg, temperature = 25 °C, [2-NP] = 50 mg L<sup>-1</sup>, [H<sub>2</sub>O<sub>2</sub>] = 500 mg L<sup>-1</sup>, and pH = 5); (B) effect of pH on the catalytic system (dose = 10 mg, [H<sub>2</sub>O<sub>2</sub>] = 500 mg L<sup>-1</sup>, temperature = 25 °C, [2-NP] = 50 mg L<sup>-1</sup>, and pH = 3–11); (C) effect of catalyst dose ([H<sub>2</sub>O<sub>2</sub>] = 500 mg L<sup>-1</sup>, temperature = 25 °C, [2-NP] = 50 mg L<sup>-1</sup>, pH = 5, and dose = 5–20 mg); and (D) effect of temperature on the Fenton-like degradation of 2-NP (temperature = 25–55 °C, [2-NP] = 50 mg L<sup>-1</sup>, pH = 5, [H<sub>2</sub>O<sub>2</sub>] = 500 mg L<sup>-1</sup>, and dose = 10 mg).

attaching metal species (eqn (2) and (3)). The auto-decomposition of H<sub>2</sub>O<sub>2</sub> in highly basic media to oxygen and water decreases the generated <sup>•</sup>OH and weakens the degradation aptitude of 2-NP, as elucidated in eqn (4). Notably, the higher adsorption percentage of 2-NP was 13.84% at pH = 5 and the pK<sub>a</sub> of 2-NP = 7.23, indicating that it is an anionic molecule in alkaline media.<sup>34,35</sup> Consequently, it was deduced that electrostatic interactions do not participate in 2-NP adsorption, and other adsorption pathways are the governing mechanisms, like pi-pi interaction, electron donor-acceptor interaction, and H-bonds.<sup>36</sup>

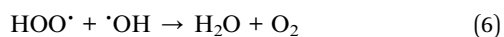
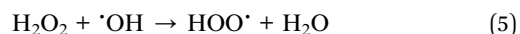


**3.2.3. Influence of the Fe<sub>3</sub>O<sub>4</sub>/MIL-88A/BC dose.** Fig. 5C shows the dosage influence of the Fenton-like Fe<sub>3</sub>O<sub>4</sub>/MIL-88A/BC catalyst on the degradation aptitude of 2-NP. The experimental results clarified a drastic enhancement in the DE of 2-NP from

50.77% to 99.27% by elevating the dose of Fe<sub>3</sub>O<sub>4</sub>/MIL-88A/BC from 5 to 20 mg. This improvement in the DE of 2-NP is most likely due to the production of greater concentrations of <sup>•</sup>OH radicals by the higher catalyst dose, which could directly attack higher concentrations of 2-NP molecules.<sup>37</sup> Moreover, increasing the Fe<sub>3</sub>O<sub>4</sub>/MIL-88A/BC catalyst dosage enhanced the adsorption percentage of 2-NP from 5.88% to 33.76% due to the plentiful adsorption groups provided by the high doses of Fe<sub>3</sub>O<sub>4</sub>/MIL-88A/BC.

**3.2.4. Influence of the temperature.** Fig. 5D shows the influence of the catalytic system temperature on the Fenton-like degradation of 2-NP by H<sub>2</sub>O<sub>2</sub> activation using Fe<sub>3</sub>O<sub>4</sub>/MIL-88A/BC. It was observed that the DE of 2-NP increased from 80.25 to 90.63% when the temperature of the catalytic system was increased from 25 to 55 °C, subsequently. Such an increment in the 2-NP degradation percentage is due to increasing the interaction between H<sub>2</sub>O<sub>2</sub> and the Fe<sub>3</sub>O<sub>4</sub>/MIL-88A/BC catalyst with increasing the temperature, which produces higher amounts of <sup>•</sup>OH radicals.<sup>38</sup> Likewise, the adsorption percentage of 2-NP increased from 13.84% to 34.76% by raising the reaction temperature from 25 to 55 °C due to fastening the Brownian motion of 2-NP molecules, which increased the number of 2-NP molecules reaching the Fe<sub>3</sub>O<sub>4</sub>/MIL-88A/BC surface.

**3.2.5. Influence of oxidant concentration.** The impact of the oxidant concentration on the efficiency of 2-NP degradation was inspected at  $\text{H}_2\text{O}_2$  concentrations ranging from 100 to 1000  $\text{mg L}^{-1}$ , as shown in Fig. 6A. The DE of 2-NP increased from 70.70% to 80.25% when the  $\text{H}_2\text{O}_2$  concentration was increased from 100 to 500  $\text{mg L}^{-1}$  because of the increase in the production of  $\cdot\text{OH}$  radicals due to the abundant concentration of  $\text{H}_2\text{O}_2$ . Nevertheless, the excess concentration of  $\text{H}_2\text{O}_2$  (over 500  $\text{mg L}^{-1}$ ) diminished the DE of 2-NP to 72.62% because higher concentrations of  $\text{H}_2\text{O}_2$  could attack the presented  $\cdot\text{OH}$  radicals in the catalytic medium and generate  $\cdot\text{OOH}$  species, as elucidated in eqn (5) and (6).



**3.2.6. Decomposition of  $\text{H}_2\text{O}_2$ .** The decomposition percentage of  $\text{H}_2\text{O}_2$  with time controls the generated amount of  $\cdot\text{OH}$  radicals and the catalytic reaction time. Consequently, the decomposition percentage of the optimal  $\text{H}_2\text{O}_2$  concentration (500  $\text{mg L}^{-1}$ ) by  $\text{Fe}_3\text{O}_4/\text{MIL-88A/BC}$  in the absence of 2-NP was examined, as shown in Fig. 6B. The results clarified that the

decomposition percentage of  $\text{H}_2\text{O}_2$  reached 98.78% after 120 minutes, implying the auspicious catalytic activity of  $\text{Fe}_3\text{O}_4/\text{MIL-88A/BC}$  and its high affinity toward activating  $\text{H}_2\text{O}_2$ .

**3.2.7. Influence of the 2-NP concentrations.** Fig. 6C demonstrates the Fenton-like activity of  $\text{Fe}_3\text{O}_4/\text{MIL-88A/BC}$  toward the degradation of 2-NP at different concentrations over 120 min. The results elucidated an improvement in the DE of 2-NP by increasing the degradation time up to 120 min, in which the 2-NP degradation percentage reached 91.04, 77.59, 66.97, and 58.99 when the initial 2-NP concentrations were 50, 100, 200, and 300  $\text{mg L}^{-1}$ , respectively. A decline in the degradation percentage of 2-NP was noticed with increasing the initial concentrations of 2-NP, most likely due to the insufficient  $\cdot\text{OH}$  radicals to degrade these high concentrations of 2-NP. Similarly, the adsorption percentage of 2-NP declined from 13.84% to 10.25%, 7.28%, and 4.85% by augmenting the 2-NP concentrations because of the lower adsorption sites of  $\text{Fe}_3\text{O}_4/\text{MIL-88A/BC}$  for high 2-NP concentrations.<sup>39</sup>

### 3.3. Kinetics study

Regression analyses for the obtained results from the Fenton-like degradation reaction of 2-NP by the  $\text{H}_2\text{O}_2/\text{Fe}_3\text{O}_4/\text{MIL-88A/}$

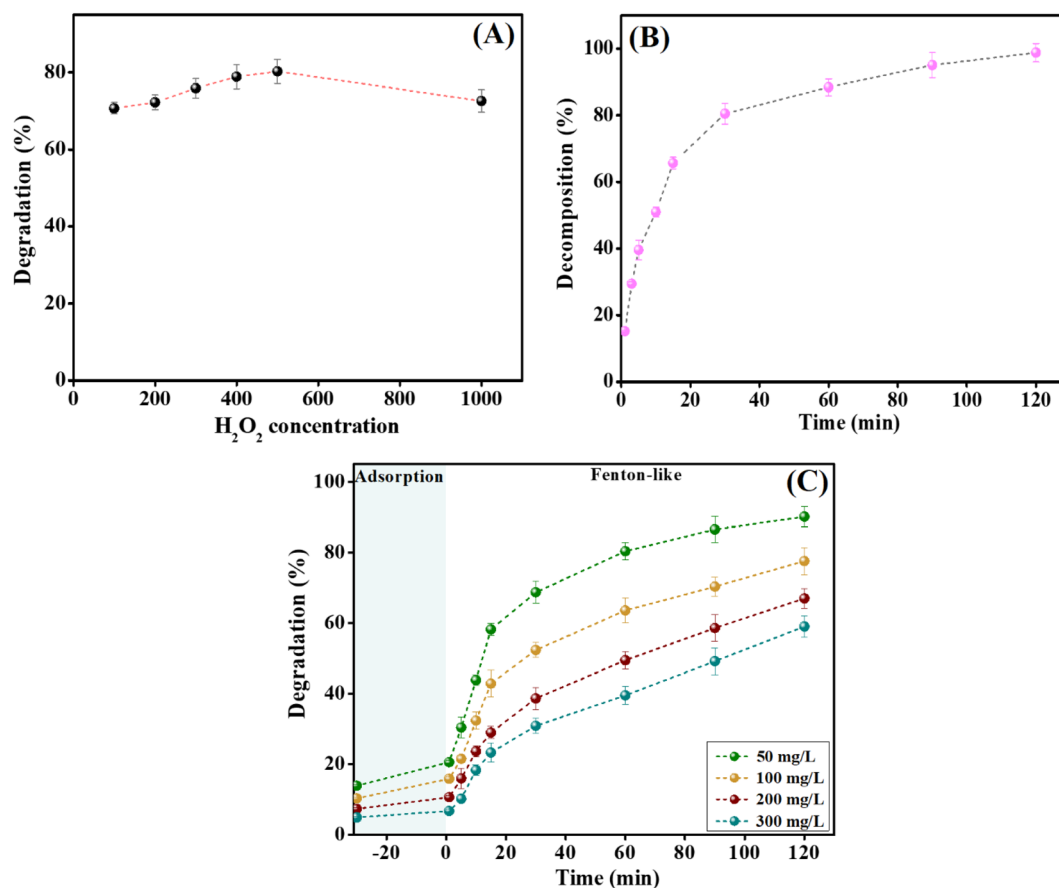


**Fig. 6** (A) Effect of oxidant concentrations ( $\text{pH} = 5$ ,  $[\text{2-NP}] = 50 \text{ mg L}^{-1}$ ,  $[\text{H}_2\text{O}_2] = 100\text{--}1000 \text{ mg L}^{-1}$ , catalyst dose = 10 mg, and temperature = 25  $^{\circ}\text{C}$ ), (B) decomposition of  $\text{H}_2\text{O}_2$  ( $[\text{2-NP}] = 50 \text{ mg L}^{-1}$ ,  $\text{pH} = 5$ ,  $[\text{H}_2\text{O}_2] = 500 \text{ mg L}^{-1}$ , catalyst dose = 10 mg, and temperature = 25  $^{\circ}\text{C}$ ); and (C) effect of 2-NP concentrations on the Fenton-like degradation efficiency ( $[\text{2-NP}] = 50\text{--}300 \text{ mg L}^{-1}$ ,  $\text{pH} = 5$ ,  $[\text{H}_2\text{O}_2] = 500 \text{ mg L}^{-1}$ , catalyst dose = 10 mg, and temperature = 25  $^{\circ}\text{C}$ ).



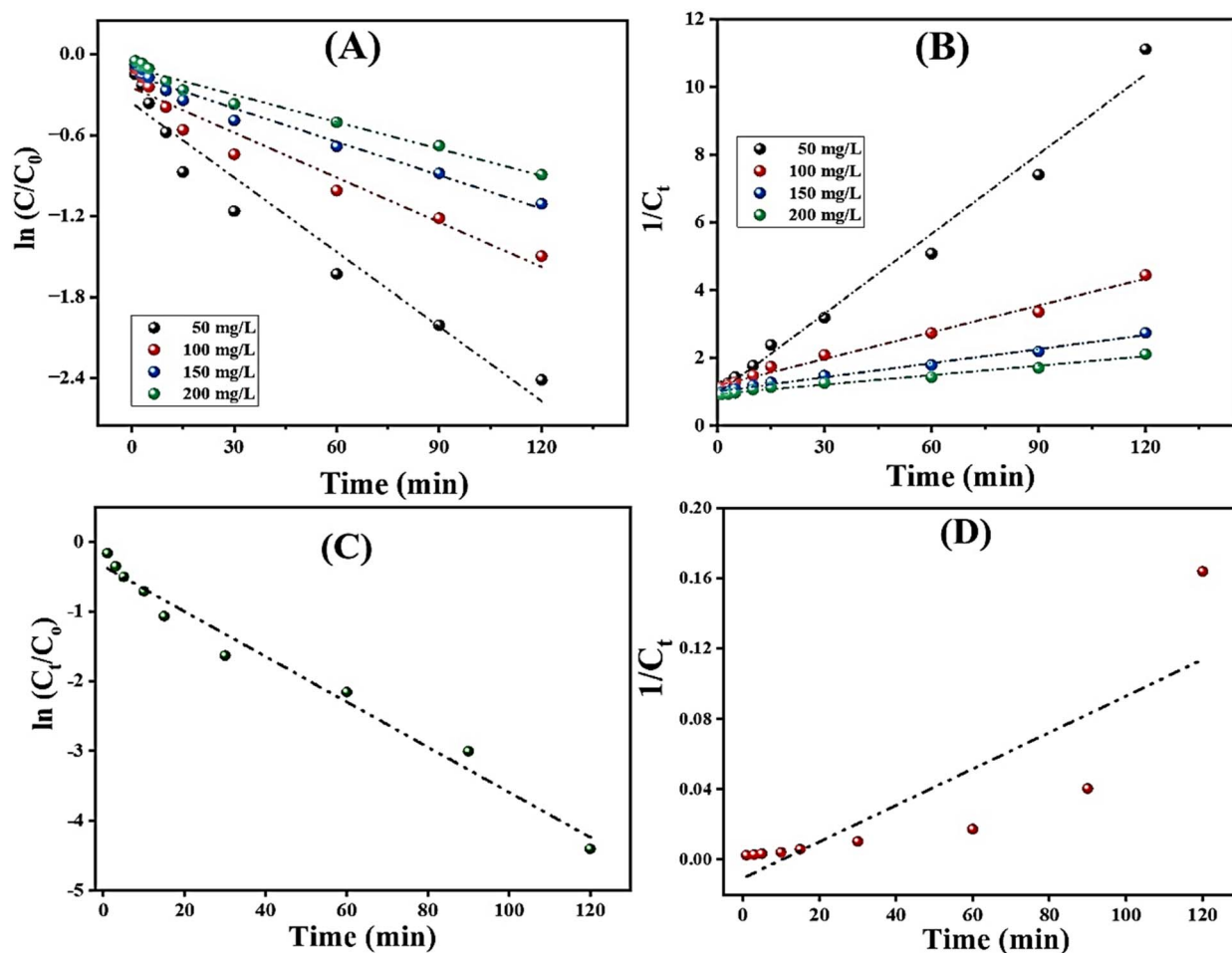


Fig. 7 Kinetic study of the Fenton-like degradation of 2-NP by the  $\text{H}_2\text{O}_2/\text{Fe}_3\text{O}_4/\text{MIL-88A}/\text{BC}$  system: (A) first-order and (B) second-order, and kinetic study of the  $\text{H}_2\text{O}_2$  decomposition: (C) first-order and (D) second-order.

BC system were performed based on First-order and Second-order (eqn (7) and (8)).

$$\ln \frac{C_t}{C_0} = -k_1 t \quad (7)$$

$$\frac{1}{C_t} = \frac{1}{C_0} + k_2 t \quad (8)$$

$C_t$  and  $C_0$  are the 2-NP concentrations at a certain time and the initial reaction time, respectively.  $k_1$  and  $k_2$  are the rate constants of First-order and Second-order processes, respectively.

As illustrated in Fig. 7A, B and Table 1, the Fenton-like degradation reaction of 2-NP by the  $\text{H}_2\text{O}_2/\text{Fe}_3\text{O}_4/\text{MIL-88A}/\text{BC}$  system fits the Second-order more than the First-order, where the derived  $R^2$  values from the Second-order are higher at varied 2-NP concentrations.<sup>40</sup> Notably,  $k_1$  and  $k_2$  are the slopes of the First-order plot ( $\ln C_t/C_0$  vs. time) and Second-order plot ( $1/C_t$  vs. time). The rate constants of the Fenton-like degradation of 2-NP based on the Second-order model were 0.0785, 0.0263, 0.0139, and 0.0093  $\text{mg L}^{-1} \text{min}^{-1}$  when the initial 2-NP concentrations were 50, 100, 200, and 300  $\text{mg L}^{-1}$ , respectively. The rate

constant of the degradation reaction of 2-NP decreased as the initial 2-NP concentration increased, which may be due to the governing of some factors, including  $\cdot\text{OH}$  production and consumption; in addition, the competition between 2-NP and its degradation intermediates.<sup>41,42</sup> The kinetic study of  $\text{H}_2\text{O}_2$  decomposition was conducted by analyzing the experimental data using first-order and second-order models (Fig. 7C and D). The derived kinetic parameters clarified the suitability of the first-order model for  $\text{H}_2\text{O}_2$  decomposition by  $\text{Fe}_3\text{O}_4/\text{MIL-88A}/$

Table 1 Derived parameter of the kinetic study of Fenton-like degradation of 2-NP

Kinetic model	Concentrations ( $\text{mg L}^{-1}$ )			
	50	100	200	300
<b>First order</b>				
$k_1$	0.0185	0.0111	0.0083	0.0067
$R^2$	0.950	0.947	0.973	0.975
<b>Second order</b>				
$k_2$	0.0785	0.0263	0.0139	0.0093
$R^2$	0.985	0.990	0.992	0.985



BC, where the  $R^2$  values of the first-order and second-order models were 0.977 and 0.692, respectively. Furthermore, the decomposition rate constant was determined as  $0.032 \text{ min}^{-1}$  using first-order kinetics calculations.

### 3.4. Fenton-like degradation mechanism

**3.4.1. Quenching test.** To determine whether the controlling reactive O-species is  $\cdot\text{OH}$  or superoxide ( $\text{O}_2^{\cdot-}$ ), quenching tests were performed using chloroform and *t*-butanol for scavenging  $\text{O}_2^{\cdot-}$  and  $\cdot\text{OH}$ , respectively.<sup>43</sup> The scavenger test (Fig. 8A) implied that  $\cdot\text{OH}$  is the dominant reactive O-species, where the Fenton-like degradation efficiency of 2-NP declined by 31.02% and 1.8% in the presence of *t*-butanol and chloroform, respectively. Such a finding denoted that the Fenton-like degradation mechanism of 2-NP by the  $\text{H}_2\text{O}_2/\text{Fe}_3\text{O}_4/\text{MIL-88A/BC}$  catalytic system follows a radical pathway, not surface oxygen vacancies.<sup>44,45</sup>

**3.4.2. XPS analysis.** Based on experimental observations, 2-NP degradation occurred *via* adsorption and a Fenton-like reaction. First, the corresponding peaks of nitrogen in the XPS survey of the  $\text{Fe}_3\text{O}_4/\text{MIL-88A/BC}$  catalyst evinced the adsorption reaction of 2-NP (Fig. 8B). This adsorption reaction between 2-NP and  $\text{Fe}_3\text{O}_4/\text{MIL-88A/BC}$  could proceed by the  $\pi$ - $\pi$  interactions

between the benzene rings in 2-NP and the catalyst. Electron donor-acceptor interactions may participate in the adsorption reaction of 2-NP by transferring electrons from the electron donor groups of  $\text{Fe}_3\text{O}_4/\text{MIL-88A/BC}$  (carboxyl and hydroxyl) to the electron acceptor nitro group of the 2-NP molecule. In addition, the hydroxyl group of 2-NP formed a coordination bond with the iron species in the  $\text{Fe}_3\text{O}_4/\text{MIL-88A/BC}$  catalyst. Moreover, H-bonds could be formed between the nitrogen and oxygen atoms of 2-NP and the hydrogen atoms of  $\text{Fe}_3\text{O}_4/\text{MIL-88A/BC}$ , whereas the oxygen atoms of the catalyst could create H-bonds with the hydrogen atoms of 2-NP molecules.

Second, the Fenton-like degradation reaction of 2-NP by  $\text{Fe}_3\text{O}_4/\text{MIL-88A/BC}$  was based on the XPS spectra that implied governing the Haber-Weiss mechanism in the degradation reaction as follows: The Fe 2p spectra (Fig. 8C) of the used and fresh  $\text{Fe}_3\text{O}_4/\text{MIL-88A/BC}$  catalysts showed a significant increment in the  $\text{Fe}^{3+}/\text{Fe}^{2+}$  ratio from 0.35 to 0.63, reflecting the consumption of  $\text{Fe}^{2+}$  in the  $\text{H}_2\text{O}_2$  activation to produce  $\cdot\text{OH}$  as represented in eqn (9). Furthermore, the XPS peaks of  $\text{Fe}^{2+}$  shifted from 710.35 and 724.16 eV to 710.30 and 723.85 eV; in addition, the peaks of  $\text{Fe}^{3+}$  also shifted from 712.24 and 727.24 eV to 713.05 and 727.03 eV. The continuous Fenton-like reaction of 2-NP requires a sustained and fast  $\text{Fe}^{3+} \rightarrow \text{Fe}^{2+}$  redox cycle; thus, the electron-rich BC can supply the redox cycle with

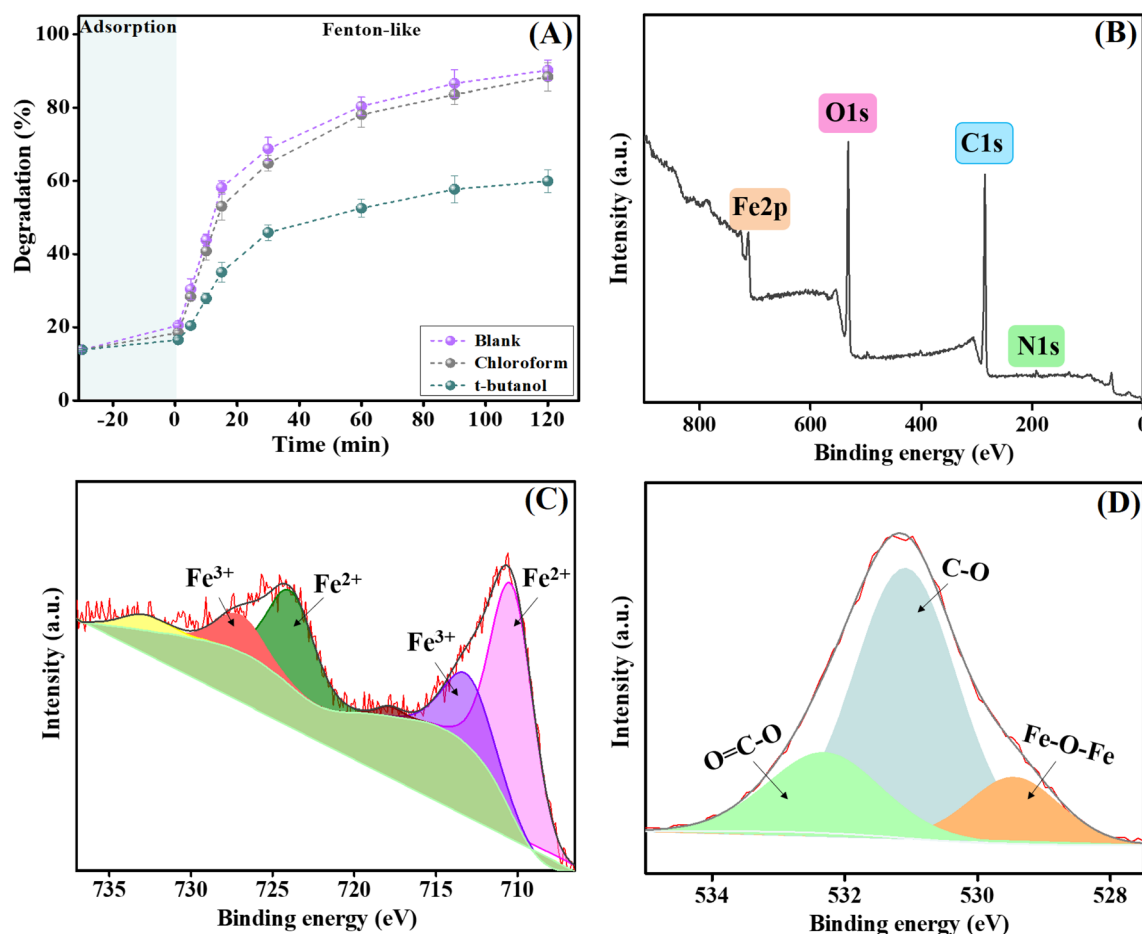
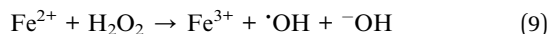


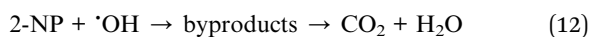
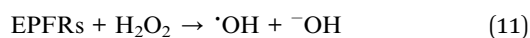
Fig. 8 (A) Quenching test of the  $\text{Fe}_3\text{O}_4/\text{MIL-88A/BC}$ , (B) XPS survey of the used  $\text{Fe}_3\text{O}_4/\text{MIL-88A/BC}$  catalyst, (C) high resolution of Fe 2p, and (D) high resolution of O 1s.



high amounts of electrons that facilitate the reduction of  $\text{Fe}^{3+}$  to  $\text{Fe}^{2+}$  (eqn (10)).



Furthermore, oxygen-centered EPFRs activate  $\text{H}_2\text{O}_2$ , generating  $\cdot\text{OH}$  radicals (eqn (11)). The O 1s spectrum (Fig. 8D) of the  $\text{Fe}_3\text{O}_4/\text{MIL-88A/BC}$  exhibited a peak shifting of the C=O, C-O, and Fe-O-Fe from 531.15, 531.18, and 529.56 eV to 531.08, 532.31, and 529.45 eV, respectively. Furthermore, the intensity of C-O and Fe-O-Fe peaks decreased, whereas the peak intensity of C=O increased after the Fenton-like degradation of 2-NP. These observations implied the participation of C=O, C-O, and Fe-O-Fe in the Fenton-like reaction of 2-NP using the  $\text{H}_2\text{O}_2/\text{Fe}_3\text{O}_4/\text{MIL-88A/BC}$  catalytic system. Hence, we could conclude the significant role of BC that is not only responsible for half of the redox cycle ( $\text{Fe}^{3+} \rightarrow \text{Fe}^{2+}$ ) but also contributes to  $\text{H}_2\text{O}_2$  activation and  $\cdot\text{OH}$  radical production. Finally, the produced  $\cdot\text{OH}$ , even by the Haber-Weiss mechanism or EPFRs-based BC, can attack o-NP molecules and degrade them to  $\text{CO}_2$  and  $\text{H}_2\text{O}$ , as clarified in eqn (12).



### 3.5. Degradation pathway

The suggested degradation pathway and the intermediates formed during the Fenton-like degradation of 2-NP onto the  $\text{Fe}_3\text{O}_4/\text{MIL-88A/BC}$  composite were analyzed using GC-MS

(Fig. 9). The  $\cdot\text{OH}$  radicals attacked 2-NP *via* two distinct pathways. Fig. 10 illustrates the possible Fenton-like degradation pathway of 2-NP on the  $\text{Fe}_3\text{O}_4/\text{MIL-88A/BC}$  composite.

In the first pathway, the hydrogen atom of the phenyl ring at position 4 was substituted, leading to the formation of nitrohydroquinone, which appeared at a retention time (RT) of 11.81 min. Subsequently, the nitro group was replaced by OH, forming a hydroquinone radical that was converted into hydroquinone (RT = 23.87 min). Hydroquinone was further oxidized to *p*-benzoquinone (RT = 10.19 min), whose oxidative cleavage ultimately yielded  $\text{CO}_2$  and water. The second pathway involved the direct substitution of the  $\text{NO}_2$  group by OH *via* a phenol radical intermediate to form catechol (RT = 21.91 min). Catechol was then oxidized to *o*-benzoquinone (RT = 16.77 min) and underwent ring opening to produce *cis-cis*-muconic acid (RT = 20.57 min). The successive oxidative cleavage of muconic acid by  $\cdot\text{OH}$  radicals resulted in the formation of maleic acid (RT = 12.87 min), followed by oxalic acid (RT = 4.57 min) and formic acid (RT = 7.44 min), which were eventually degraded into carbon dioxide and water. Fig. 10 illustrates the possible Fenton-like degradation pathway of 2-NP on the  $\text{Fe}_3\text{O}_4/\text{MIL-88A/BC}$  composite.

### 3.6. Stability of the $\text{Fe}_3\text{O}_4/\text{MIL-88A/BC}$ catalyst

To confirm the stability of  $\text{Fe}_3\text{O}_4/\text{MIL-88A/BC}$ , it was crucial to examine the metal leaching after the Fenton-like reaction and study the recyclability of the catalyst.

**3.6.1. Recyclability study.** A cycling test was executed for five cycles of Fenton-like degradation of 2-NP to investigate the recyclability of the  $\text{Fe}_3\text{O}_4/\text{MIL-88A/BC}$  catalyst (Fig. 11A). Surprisingly, the results observed the superb recyclability of  $\text{Fe}_3\text{O}_4/\text{MIL-88A/BC}$ , where its activity decreased by 8.54% after

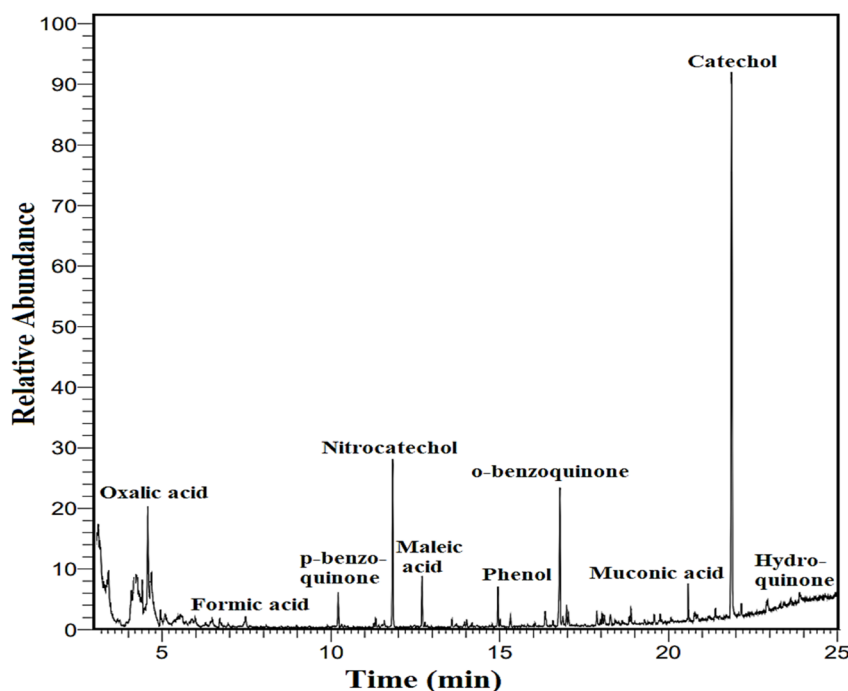


Fig. 9 GC-MS of 2-NP after Fenton-like degradation by the  $\text{Fe}_3\text{O}_4/\text{MIL-88A/BC}$  composite.



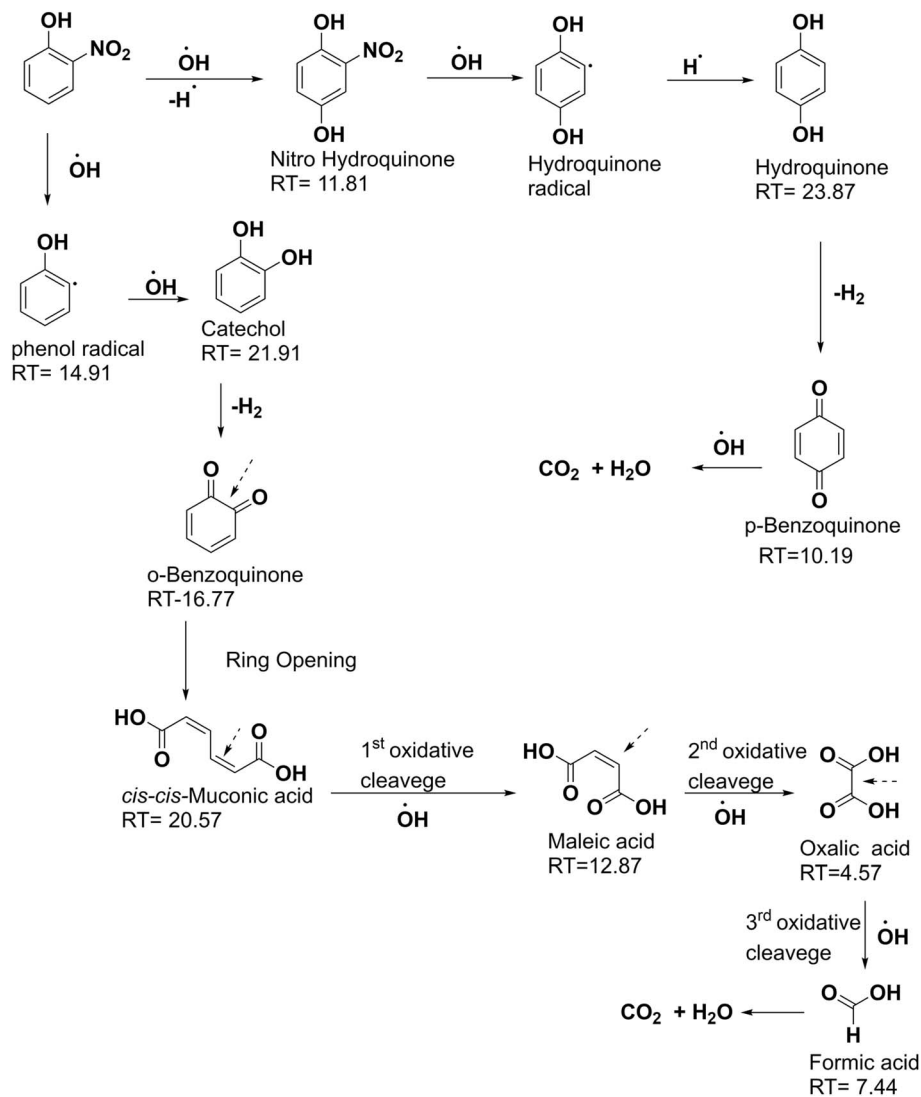


Fig. 10 Schematic representation of the degradation of 2-NP by the  $\text{Fe}_3\text{O}_4/\text{MIL-88A/BC}$  composite.

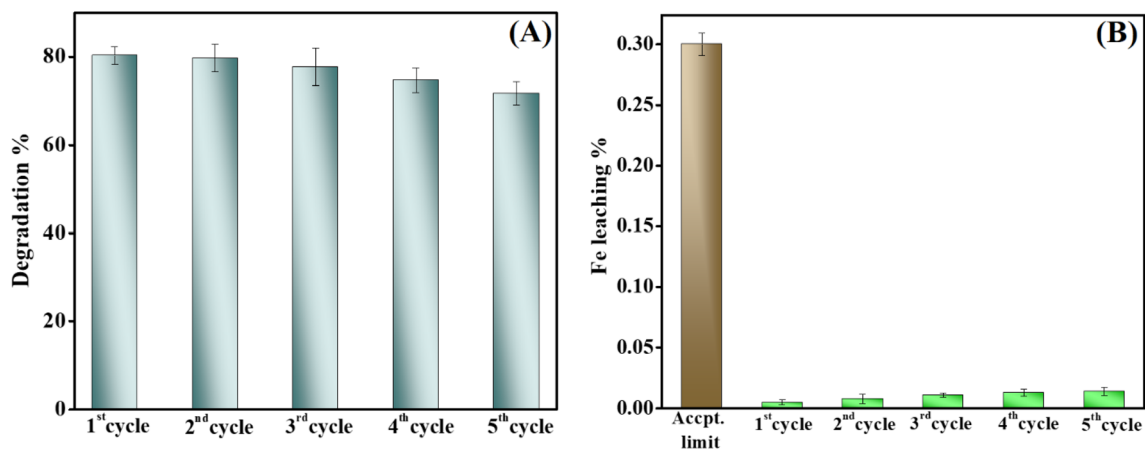


Fig. 11 (A) Cycling test of the  $\text{Fe}_3\text{O}_4/\text{MIL-88A/BC}$  catalyst for five 2-NP degradation cycles and (B) leaching test of Fe species from the  $\text{Fe}_3\text{O}_4/\text{MIL-88A/BC}$  composite during the five degradation cycles.



the 5th cycle. This propitious recyclability owes to the catalyst; the magnetic character of  $\text{Fe}_3\text{O}_4/\text{MIL-88A/BC}$  provides perfect and fast separation using a magnet without weight loss. Meanwhile, the decline in the catalytic activity after the o-NP degradation cycles may be explained by the possible adsorption interactions between o-NP and  $\text{Fe}_3\text{O}_4/\text{MIL-88A/BC}$ , which resulted in incomplete recovery of the catalyst, since some o-NP molecules were still attached to the active groups of the catalyst. In addition, the regeneration of  $\text{Fe}^{2+}$  could not occur completely because not all  $\text{Fe}^{3+}$  species were reduced to  $\text{Fe}^{2+}$ . Furthermore, the expected Fe leaching from  $\text{Fe}_3\text{O}_4/\text{MIL-88A/BC}$  after the sequential Fenton-like degradation of o-NP could impact the efficacy of the catalyst.

**3.6.2. Metal leaching.** XPS surveys of authentic and used  $\text{Fe}_3\text{O}_4/\text{MIL-88A/BC}$  catalysts revealed an increment in the carbon content from 49.56% to 61.85% and a diminution in oxygen percentage from 41.88% to 27.73%, which may be attributed to the conversion of some oxygen-centered EPFRs to carbon-centered EPFRs after the catalytic degradation reaction of 2-NP.<sup>17</sup> The appearance of a tiny peak belonging to N1s (1.98%) is attributed to the present nitro group in 2-NP. Interestingly, the Fe leaching percentage from  $\text{Fe}_3\text{O}_4/\text{MIL-88A/BC}$  after the Fenton-like degradation of 2-NP was approximately 1.97%, confirming the viability of the chemical structure of the as-fabricated catalyst. For a further indication of the chemical stability of  $\text{Fe}_3\text{O}_4/\text{MIL-88A/BC}$ , the Fe leaching percentage was evaluated by ICP-OES, as shown in Fig. 11B. The Fe leaching percentage from the  $\text{Fe}_3\text{O}_4/\text{MIL-88A/BC}$  catalyst after Fenton-like degradation of 2-NP was 0.005, 0.008, 0.011, 0.0013, and 0.014  $\text{mg L}^{-1}$ . The acceptable limit of Fe ions in drinking water is 0.3  $\text{mg L}^{-1}$  according to the USEPA. This finding not only confirms the chemical composition stability of  $\text{Fe}_3\text{O}_4/\text{MIL-88A/BC}$  but also indicates the eco-friendliness of the catalyst.

## 4. Conclusion

$\text{Fe}_3\text{O}_4/\text{MIL-88A/BC}$  was successfully fabricated, and its physical and chemical characteristics were identified by various characterization analyses, including SEM, ZP, XRD, XPS, and FTIR. The SEM image revealed the diamond-shaped MIL-88A fabricated using the solvothermal approach. The FTIR and XRD patterns of  $\text{Fe}_3\text{O}_4/\text{MIL-88A/BC}$  demonstrated a good combination of  $\text{Fe}_3\text{O}_4$ , MIL-88A, and BC inside the composite structure. The results of the laboratory experiments showed that the DE of 2-NP by the  $\text{H}_2\text{O}_2/\text{Fe}_3\text{O}_4/\text{MIL-88A/BC}$  catalytic system reached 91.04% at pH = 5,  $\text{H}_2\text{O}_2$  concentration = 500  $\text{mg L}^{-1}$ ,  $\text{Fe}_3\text{O}_4/\text{MIL-88A/BC}$  = 10 mg, and 120 min. The quenching test deduced 2-NP degradation *via* the radical pathway, with  $\cdot\text{OH}$  as the main reactive O-species. The XPS analysis of pristine and used  $\text{Fe}_3\text{O}_4/\text{MIL-88A/BC}$  suggested the occurrence of the Fenton-like degradation of 2-NP by the Haber–Weiss mechanism and EPFRs-based BC. Notably, the ability of BC to donate electrons enabled it to be the controller in the half of the redox cycle ( $\text{Fe}^{3+} \rightarrow \text{Fe}^{2+}$ ) and the continuity of the Fenton-like degradation of 2-NP.

Based on our in-depth study, we recommend our catalyst as a superb catalyst for Fenton-like reactions, taking into

consideration increasing the number of transition metals in the catalyst to expand the redox cycle by doping metal species, fabricating bimetallic/binary MOF, or adding layered double/triple hydroxide to the catalyst matrix. These transition metals boost the concentration of the generated  $\cdot\text{OH}$  radicals and work together with BC to recover the  $\text{Fe}^{2+}$  ions, thereby further improving the degradation efficacy and catalyst recyclability. Furthermore, the Fenton/Fenton-like degradation of 2-NP requires further investigation because there is a shortage of published research highlighting this topic. Excessive studies are essential to propose other degradation pathways for 2-NP and to examine the toxicity of the produced intermediates.

## Data availability

The data that support the findings of this study are available from the corresponding author upon reasonable request.

## Conflicts of interest

There are no conflicts to declare.

## Funding

This work was supported by the Deanship of Scientific Research, Vice Presidency for Graduate Studies and Scientific Research, King Faisal University, Saudi Arabia (Project No. KF252061).

## Acknowledgements

JA and MSA acknowledge “the Deanship of Scientific Research, Vice Presidency for Graduate Studies and Scientific Research, King Faisal University, Saudi Arabia, for financial support under the annual funding track [KF252061].

## References

- 1 B. S. Marques, K. Dalmagro, K. S. Moreira, M. L. Oliveira, S. L. Jahn, T. A. de Lima Burgo and G. L. Dotto, *J. Alloys Compd.*, 2020, **838**, 155628.
- 2 A. M. Omer, A. S. Eltaweil, A. M. Abdelhamed, E. M. Abd El-Monaem and G. M. El-Subruiti, *Sci. Rep.*, 2024, **14**, 14463.
- 3 D. Ewis, M. M. Ba-Abbad, A. Benamor, N. Mahmud, M. Nasser, M. El-Naas and A. W. Mohammad, *Int. J. Environ. Res.*, 2022, **16**, 23.
- 4 D. Khan, J. Kuntail and I. Sinha, *J. Mol. Graphics Modell.*, 2022, **116**, 108251.
- 5 Y. Yang, Y. Gu, H. Lin, B. Jie, Z. Zheng and X. Zhang, *J. Colloid Interface Sci.*, 2022, **608**, 2884–2895.
- 6 A. S. Eltaweil, A. M. Galal, E. M. Abd El-Monaem, N. Al Harby and M. El Batouti, *Nanomaterials*, 2024, **14**.
- 7 J. Lu, M. Yue, W. Cui, C. Sun and L. Liu, *Colloids Surf., A*, 2022, **655**, 130222.
- 8 Y. Liu and J. Wang, *Chem. Eng. J.*, 2023, **466**, 143147.
- 9 E. M. Abd El-Monaem, A. M. Omer and A. S. Eltaweil, *J. Polym. Environ.*, 2024, **32**, 2075–2090.



- 10 J. Tang and J. Wang, *Environ. Sci. Technol.*, 2018, **52**, 5367–5377.
- 11 V. P. Viswanathan, S. V. Mathew, D. P. Dubal, N. N. Adarsh and S. Mathew, *ChemistrySelect*, 2020, **5**, 7534–7542.
- 12 H. Fu, X.-X. Song, L. Wu, C. Zhao, P. Wang and C.-C. Wang, *Mater. Res. Bull.*, 2020, **125**, 110806.
- 13 S. M. Shaheen, N. K. Niazi, N. E. Hassan, I. Bibi, H. Wang, D. C. Tsang, Y. S. Ok, N. Bolan and J. Rinklebe, *Int. Mater. Rev.*, 2019, **64**, 216–247.
- 14 J. Wang and S. Wang, *J. Cleaner Prod.*, 2019, **227**, 1002–1022.
- 15 E. M. Abd El-Monaem, A. M. Omer, G. M. El-Subruiti, M. S. Mohy-Eldin and A. S. Eltaweil, *Biomass Convers. Biorefin.*, 2024, **14**, 1697–1709.
- 16 R. Deng, H. Luo, D. Huang and C. Zhang, *Chemosphere*, 2020, **255**, 126975.
- 17 X. Ruan, Y. Sun, W. Du, Y. Tang, Q. Liu, Z. Zhang, W. Doherty, R. L. Frost, G. Qian and D. C. Tsang, *Bioresour. Technol.*, 2019, **281**, 457–468.
- 18 M. Jin, M. Long, H. Su, Y. Pan, Q. Zhang, J. Wang, B. Zhou and Y. Zhang, *Environ. Sci. Pollut. Res.*, 2017, **24**, 1926–1937.
- 19 R. C. Costa, F. C. Moura, J. Ardisson, J. Fabris and R. Lago, *Appl. Catal., B*, 2008, **83**, 131–139.
- 20 G. Fang, J. Gao, C. Liu, D. D. Dionysiou, Y. Wang and D. Zhou, *Environ. Sci. Technol.*, 2014, **48**, 1902–1910.
- 21 Y. Pan, M. Zhou, X. Li, L. Xu, Z. Tang and M. Liu, *Sep. Purif. Technol.*, 2016, **169**, 83–92.
- 22 L. Yu, X. Yang, Y. Ye and D. Wang, *RSC Adv.*, 2015, **5**, 46059–46066.
- 23 L. Xu and J. Wang, *Environ. Sci. Technol.*, 2012, **46**, 10145–10153.
- 24 G. Fang, C. Zhu, D. D. Dionysiou, J. Gao and D. Zhou, *Bioresour. Technol.*, 2015, **176**, 210–217.
- 25 G. Ren, K. Zhao and L. Zhao, *RSC Adv.*, 2020, **10**, 39973–39980.
- 26 E. M. Abd El-Monaem, N. Al Harby, M. E. Batouti and A. S. Eltaweil, *Nanomaterials*, 2023, **14**, 54.
- 27 X. Liao, F. Wang, F. Wang, Y. Cai, Y. Yao, B.-T. Teng, Q. Hao and L. Shuxiang, *Appl. Catal., B*, 2019, **259**, 118064.
- 28 F. Sang, Z. Yin, W. Wang, E. Almatrafi, Y. Wang, B. Zhao, J. Gong, C. Zhou, C. Zhang and G. Zeng, *J. Cleaner Prod.*, 2022, **378**, 134459.
- 29 J.-H. Park, J. J. Wang, R. Xiao, N. Tafti, R. D. DeLaune and D.-C. Seo, *Bioresour. Technol.*, 2018, **249**, 368–376.
- 30 S. Zhao, Y. Li, M. Wang, B. Chen, Y. Zhang, Y. Sun, K. Chen, Q. Du, Z. Jing and Y. Jin, *Microporous Mesoporous Mater.*, 2022, **345**, 112241.
- 31 A. M. Omer, M. El-Sayed, E. M. Abd El-Monaem, G. M. El-Subruiti and A. S. Eltaweil, *Int. J. Biol. Macromol.*, 2023, **253**, 127437.
- 32 A. S. Eltaweil, S. S. Bakr, E. M. Abd El-Monaem and G. M. El-Subruiti, *Environ. Sci. Pollut. Res.*, 2023, **30**, 75332–75348.
- 33 E. M. Abd El-Monaem, M. Hosny and A. S. Eltaweil, *Chem. Eng. Sci.*, 2024, **287**, 119707.
- 34 B. S. Marques, K. Dalmagro, K. S. Moreira, M. L. Oliveira, S. L. Jahn, T. A. De Lima Burgo and G. L. Dotto, 2020.
- 35 H. Ma, Z. Xu, W. Wang, X. Gao and H. Ma, *RSC Adv.*, 2019, **9**, 39282–39293.
- 36 J. Chen, X. Sun, L. Lin, X. Dong and Y. He, *Chin. J. Chem. Eng.*, 2017, **25**, 775–781.
- 37 A. Jawad, J. Lang, Z. Liao, A. Khan, J. Ifthikar, Z. Lv, S. Long, Z. Chen and Z. Chen, *Chem. Eng. J.*, 2018, **335**, 548–559.
- 38 X. Li, K. Cui, Z. Guo, T. Yang, Y. Cao, Y. Xiang, H. Chen and M. Xi, *Chem. Eng. J.*, 2020, **379**, 122324.
- 39 A. S. Eltaweil, N. Al Harby, A. I. Osman, M. Alrasheedi, Y. Su and E. M. Abd El-Monaem, *J. Ind. Eng. Chem.*, 2025, **143**, 704–716.
- 40 N. A. Youssef, S. A. Shaban, F. A. Ibrahim and A. S. Mahmoud, *Egypt. J. Pet.*, 2016, **25**, 317–321.
- 41 T. Geng, J. Yan, B. Li, H. Yan, L. Guo, Q. Sun, Z. Guan, C. Zhao, J. Xu and W. Wang, *Results Chem.*, 2024, **11**, 101795.
- 42 J. Singh, J. Yang, Y. Chang and J. Koduru, *Chem. Eng. J.*, 2017, **307**, 74–84.
- 43 G. Rózsa, M. Náfrádi, T. Alapi, K. Schrantz, L. Szabó, L. Wojnárovits, E. Takács and A. Tungler, *Appl. Catal., B*, 2019, **250**, 429–439.
- 44 Y. Wu, X. Li, H. Zhao, F. Yao, J. Cao, Z. Chen, F. Ma, D. Wang and Q. Yang, *Chemosphere*, 2022, **287**, 132061.
- 45 X. Li, H. Zhou, R. Qian, X. Zhang and L. Yu, *Chin. Chem. Lett.*, 2025, **36**, 110036.

